Materials Advances

ROYAL SOCIETY OF CHEMISTRY

PAPER

View Article Online
View Journal | View Issue

Cite this: *Mater. Adv.*, 2025, 6, 9545

Chirality-driven dimensionality and broadband emission in lead bromide perovskites

Cássio C. S. Soares,[ab] Carlos Mera Acosta,[a] Fábio F. Ferreira,[a] Aryane Tofanello,[a] Mayra A. P. Gómez,[b] Alejandro P. Ayala,[b] J. R. Toledo,[c] Yara Galvão Gobato,[c] Maykon A. Lemes,[a] Carlos W. A. Paschoal[b] and José A. Souza*[a]

Incorporating chiral organic cations into hybrid organic–inorganic perovskites (HOIPs) offers a unique strategy for tailoring structural dimensionality and modulating photophysical properties. Here, we report that lead bromide perovskites synthesized with chiral ligands *R*- and *S*-α-methylbenzylammonium (MBA) lead to the formation of two-dimensional (2D) Ruddlesden–Popper structures, while the racemic mixture induces the formation of a hydrated 1D phase, (Rac-MBA)$_3$PbBr$_5$·H$_2$O. DFT calculations show that this transition is driven by electrostatic strain from opposing chiral distortions, which favor octahedral connections with compensated dipoles. Water molecules occupy sites between inorganic chains and mediate hydrogen bonds, stabilizing the 1D motif and relieving strain from racemic reordering. These waters form symmetry-related interstitial networks that mirror the chiral organization, acting as electrostatic compensators in the absence of lateral Pb–Br bonding. Theoretical and experimental characterization studies show that the hydrated structure is energetically stable only when four symmetry-related 1D chains and water are present; otherwise, it becomes metallic or unstable. Electronic calculations reveal Rashba-type spin splitting in chiral phases, and the formation of Br-derived mid-gap states and a Fermi level near the conduction band in the racemic compound. This hydrated phase exhibits pronounced broadband photoluminescence attributed to self-trapped excitons (STEs), and temperature-dependent optical and structural studies reveal that exciton localization and emission dynamics are closely related to octahedral distortions and hydration effects. Our findings demonstrate that stereochemical engineering can offer a robust strategy to modulate dimensionality and optical functionality, with implications for broadband light-emitting applications.

Received 15th September 2025,
Accepted 14th October 2025

DOI: 10.1039/d5ma01061f

rsc.li/materials-advances

1. Introduction

Hybrid organic–inorganic perovskites (HOIPs) have attracted significant attention due to their exceptional optoelectronic properties and structural tunability, which make them promising candidates for applications in photovoltaics, light-emitting devices, sensors, and photodetectors.[1–4] In particular, low-dimensional lead halide perovskites have emerged as promising materials due to their quantum confinement and dielectric screening effects, enhanced exciton–phonon interactions, and structural versatility afforded by organic spacer engineering.[5–7] One of many strategies to engineer these properties lies in the molecular design of the organic spacer cation, which not only dictates the dimensionality of the perovskite lattice but also modulates the electronic structure, exciton dynamics, and lattice stability.[8–11]

The incorporation of chiral organic cations introduces new degrees of freedom in perovskite physics.[12–15] Beyond structural templating, chirality can be transferred from the organic to the inorganic framework, potentially leading to novel optical activity, spin-selective transport, and enhanced light–matter interactions.[16–20] Enantiopure organic cations favor the formation of well-ordered 2D Ruddlesden–Popper structures. At the same time, racemic mixtures can often result in disordered assemblies introducing packing frustration and symmetry breaking, thereby leading to different phases and new photophysical behavior.[21,22] However, the mechanisms by which racemic and enantiopure cations affect the structural dimensionality and enable broadband photoluminescence, particularly through chiral strain and hydration effects, remain to be elucidated.

Here, we present a comparative study of lead bromide perovskites incorporating *R*-, *S*-, and racemic α-methylbenzylammonium

[a] Center for Human and Natural Sciences, Federal University of ABC, Santo André, Brazil. E-mail: joseantonio.souza@ufabc.edu.br
[b] Department of Physics, Federal University of Ceará, Fortaleza, Brazil
[c] Federal University of São Carlos, Department of Physics, São Carlos, Brazil

(MBA) cations. Our results demonstrate that while enantiopure MBA leads to the formation of highly ordered 2D perovskites, the racemic mixture promotes the formation of a 1D hydrated phase, (Rac-MBA)$_3$PbBr$_5$·H$_2$O. This effect is accompanied by the emergence of broadband self-trapped exciton (STE) emission, in contrast to the narrow-band excitonic emission observed in the 2D chiral counterparts. This behavior arises from the combined effects of molecular chirality, packing frustration, exciton–phonon coupling, and structural and electronic responses to hydration. Density functional theory calculations further reveal Rashba-type spin splitting in the chiral phases and the formation of mid-gap Br-derived states in the 1D racemic structure. These states are stabilized electrostatically by symmetry-related interstitial water molecules, which mediate hydrogen bonding and enforce local dipole compensation. Structural and temperature-dependent optical studies reveal that racemic distribution and hydration play a key role not only in stabilizing the 1D framework, but also in modulating the bandgap and enabling phonon-assisted recombination. Our results establish a direct link between molecular stereochemistry, dimensional control, and electronic band structure. These findings highlight the role of stereochemical engineering in controlling both the dimensionality and optoelectronic properties of HOIPs, offering new design principles for devices based on chiral and racemic molecular components.

2. Experimental section

Materials

Lead(II) oxide (PbO, ≥99.0%), hydrobromic acid (HBr, 48 wt%), diethyl ether (≥99.9%), (*S*)-(−)-α-methylbenzylamine (*S*-MBA, 98%), (*R*)-(+)-α-methylbenzylamine (*R*-MBA, ≥99.0%), and (±)-α-methylbenzylamine (Rac-MBA, 99.0%) were purchased from Sigma-Aldrich and used without further purification.

Synthesis

In a 25 mL beaker with a magnetic stir bar, 1 mmol PbO was dissolved in 5 mL of HBr at 120 °C under vigorous stirring for 15 minutes. After dissolution, 2 mmol *S*-MBA, *R*-MBA, and Rac-MBA were added dropwise. The solutions were then stirred for 1 hour before being slowly cooled to room temperature, resulting in colorless microcrystals that were washed several times with diethyl ether to remove any residual solvent and left to dry overnight. Thin films were prepared by dissolving 5 mg of each enantiomer-based perovskite sample in 20 μL of DMF, followed by drop-casting the solution onto a quartz substrate at 65 °C for 1 hour.

Instrumentation

Powder X-ray diffraction (PXRD) measurements were performed on a STADI-P (Stoe®, Darmstadt, Germany) diffractometer operating in Debye–Scherrer geometry. The instrument was equipped with a curved Ge(111) monochromator to select the CuKα$_1$ radiation (λ = 1.54056 Å). The powdered sample was loaded into a 0.3 mm diameter glass capillary tube. Measurements were performed at several discrete temperatures, specifically at 80 K, 100 K, 120 K, 200 K, 330 K, 380 K, 400 K, 380 K, 360 K, 340 K, 320 K, and 300 K, with the temperature being stabilized and controlled using an Oxford Cryostream 1000 series cryostat. Diffraction patterns were recorded in the $2.000^\circ \leq 2\theta \leq 93.335^\circ$ angular range, with a step size of 0.015° and an acquisition time of 50 s for each 1.05° scan window. Structural analysis and Rietveld refinements were conducted using TOPAS-Academic v.7 software.[23] The (*R*-/*S*-MBA)$_2$PbBr$_4$ structures were simulated for the refinements from the crystallographic information file of (*R*-/*S*-MBA)$_2$PbI$_4$ (CCDC 607740 and 607741), where the halides were replaced by bromide. The (*R*-/*S*-MBA)PbBr$_3$ (CCDC 1877050 and 1877054) structure was also used in the refinements. Single crystal X-ray diffraction measurements were performed on a Bruker D8 Venture X-ray diffractometer equipped with a Photon II Kappa detector and a MoKα$_1$ radiation (λ = 0.71073 Å) microfocus source. The crystal was chosen and mounted on a MiTeGen MicroMount using immersion oil. APEX 6 software was used for unit cell determination and data collection. The data reduction and global cell refinement were conducted using the Bruker SAINT$^+$ software package, and a numerical absorption correction was performed using SADABS.[24,25] The structure was solved by the intrinsic phasing method using SHELXT,[26] allowing the location of most non-hydrogen atoms. The remaining non-hydrogen atoms were located from the difference Fourier maps calculated from successive full-matrix least-squares refinement cycles on F^2 with SHELXL[27] and refined using anisotropic displacement parameters under the graphical interface Olex2.[28] Hydrogen atoms were placed according to geometrical criteria and treated using the riding model. Crystallographic data for the structures reported here have been deposited with the Cambridge Crystallographic Data Centre. CCDC 2466728 contains the supplementary crystallographic data for this paper. Crystallographic illustrations were obtained using VESTA software.[29] Scanning electron microscopy analysis was performed using a JSM-6010LA microscope. Circular dichroism spectra were collected using a JASCO J-815 spectropolarimeter. UV-visible absorption spectra were recorded using a Thermo Fisher Evolution 220 spectrophotometer. Room-temperature photoluminescence measurements were carried out using a Horiba FluoroMax Plus spectrofluorometer. Low temperature optical measurements were performed using a closed-cycle Janis CCS-150 cryostat. A continuous-wave (cw) linearly polarized CNI laser with a photon energy of 3.88 eV (320 nm) was used to excite the sample. The photoluminescence signal was focused on an Andor Shamrock SR-500i spectrometer coupled with an Andor CCD (iDus DU420A-BU). Differential scanning calorimetry was performed on a Q2000 calorimeter (TA Instruments). The experiment was conducted at a rate of 5 °C min^{-1} over the temperature range of 70–180 °C under a nitrogen atmosphere using 5 mg of the sample for each run. Raman spectroscopy was performed using a Jobin Yvon T64000 spectrometer equipped with an Olympus microscope and an LN$_2$-cooled CCD to detect the emitted radiation from the samples in a single mode and a Krypton ion laser operating at a wavelength of 633 nm.

Density functional theory simulations

The *ab initio* calculations were performed within the DFT using the Perdew–Burke–Ernzerhof (PBE) generalized gradient approximation exchange–correlation functional[30] as implemented in the Vienna *ab initio* simulation package.[31,32] We included the spin–orbit interaction in all calculations to introduce the effect of the noncollinear spin and relativistic corrections with a cutoff energy of 500 Ry and *k*-point sampling of $6 \times 6 \times 3$ for the experimental atomic configurations at 304 K. The electronic structure was minimized with a converge criterion of 10^{-5} eV, while the geometry and forces were set to the experimental configuration without additional atomic relaxation.

3. Results and discussion

Lead bromide-based HOIPs were synthesized using *R*-/*S*-/Rac-α-methylbenzylammonium (*R*-/*S*-/Rac-MBA) as the organic cation spacer. These molecules comprise a secondary carbon bonded to a phenyl, a methyl and a protonated ammonium group, as illustrated in Fig. S1. In order to synthesize (*R*-/*S*-/Rac-MBA)$_2$PbBr$_4$, we used the slow evaporation method with an aqueous HBr solution of stoichiometric amounts of PbO and *R*-/*S*-/Rac-MBA in a 1 : 2 ratio as described in the Experimental section. Fig. 1a and b shows the scanning electron microscopy (SEM) images of the obtained samples. The *R*-/*S*-MBA based perovskites were in the form of flat needle-like crystals ranging from 50 to 150 μm with lamellar conformation. In contrast, the use of the racemic mixture yielded prolonged block-shaped crystals with axes ranging from 50 to 100 μm with three well-defined dimensions. Fig. 1c and d shows the room-temperature XRD pattern along with Rietveld refinement of the as-prepared (*R*-/*S*-MBA) sample. Both compounds crystallize as mirror images of 2D Ruddlesden–Popper perovskites with an orthorhombic crystal structure and a Sohncke $P2_12_12_1$ space group,[33,34] revealing inorganic layers of corner-sharing PbBr$_6$ octahedra in the (0 0 2*l*) planes (where *l* is an integer) separated by bilayers of *R*-/*S*-MBA cations along the *c* axis as shown in Fig. 2a. Weak van der Waals interactions stabilize the organic layers. In contrast, the bonding between the organic and inorganic layers is mediated by hydrogen bonding. The powder XRD also detected a very small amount of the (*R*-/*S*-MBA)PbBr$_3$ 1D phase. The experimental PXRD patterns of (*R*-/*S*-MBA)$_2$PbBr$_4$, along with the simulated single-crystal XRD patterns of both the 2D phase and the (*R*-/*S*-MBA)PbBr$_3$ phases, are shown in Fig. S2 for comparison.

Although the same synthesis procedure was adopted to synthesize 2D perovskites with the racemic mixture in the organic cation site, the Bragg reflections do not belong to the 2D orthorhombic crystal structure as observed for chiral molecules. On the other hand, single-crystal X-ray diffraction (SCXRD) of the obtained microcrystals revealed the formation of a completely different crystal phase—a monoclinic monohydrated 1D (Rac-MBA)$_3$PbBr$_5$·H$_2$O perovskite belonging to the *C*2/*c* space group that was first reported by Billing and Lemmerer,[21,35] as shown in Fig. 1e. This MBA-based perovskite

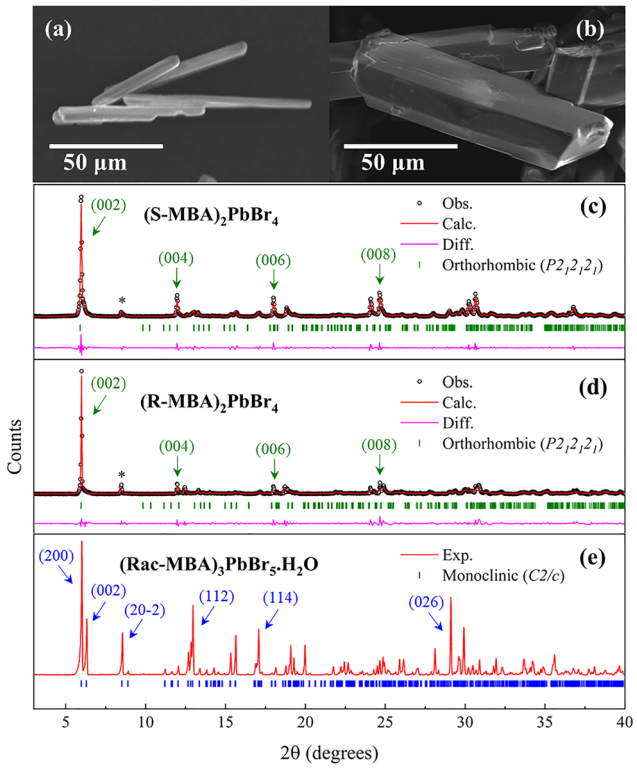

Fig. 1 SEM images of the (a) (*S*-MBA)$_2$PbBr$_4$ and (b) (Rac-MBA)$_3$PbBr$_5$·H$_2$O microcrystals. Powder XRD patterns along with Rietveld refinements for the chiral perovskites: (c) (*S*-MBA)$_2$PbBr$_4$ and (d) (*R*-MBA)$_2$PbBr$_4$. Tick marks below the XRD pattern indicate the expected Bragg reflection positions considering the orthorhombic phase with $P2_12_12_1$ space group symmetry for both samples. Asterisks (*) stand for the (002) plane from traces of (*R*-/*S*-MBA)PbBr$_3$. (e) Powder XRD and simulated Bragg reflections considering a monoclinic monohydrated 1D (Rac-MBA)$_3$PbBr$_5$·H$_2$O phase with a *C*2/*c* space group symmetry. Green and blue arrows indicate the most intense diffraction peaks that distinguish the 2D and monohydrated 1D perovskites.

has chains of corner-sharing PbBr$_6$ octahedra running along the *b* axis in a zig–zag pattern. Organic cations surround each chain arranged radially, with their ammonium heads directed toward the chains to form hydrogen bonds with water molecules positioned between adjacent chains, as illustrated in Fig. 2b. Comparative lattice parameters of the (*R*-/*S*-MBA)$_2$PbBr$_4$ and (Rac-MBA)$_3$PbBr$_5$·H$_2$O perovskites are displayed in Table S1, and SCXRD data together with refinement parameters are available in Table S2.

Although there are some examples of chiral halide perovskites where structures with different dimensionalities appear upon incorporating racemic cations,[36,37] the underlying mechanism of such phenomena remains not fully defined. The formation of the 1D (Rac-MBA)$_3$PbBr$_5$·H$_2$O structure, instead of the 2D phases observed for enantiopure (*R*-/*S*-MBA)$_2$PbBr$_4$ crystals, could be attributed to a combination of electrostatic repulsion and molecular distortions introduced by the racemic mixture. While enantiopure MBA cations adopt a uniform orientation that enables ordered bilayer formation through directional hydrogen bonding and efficient packing, as shown

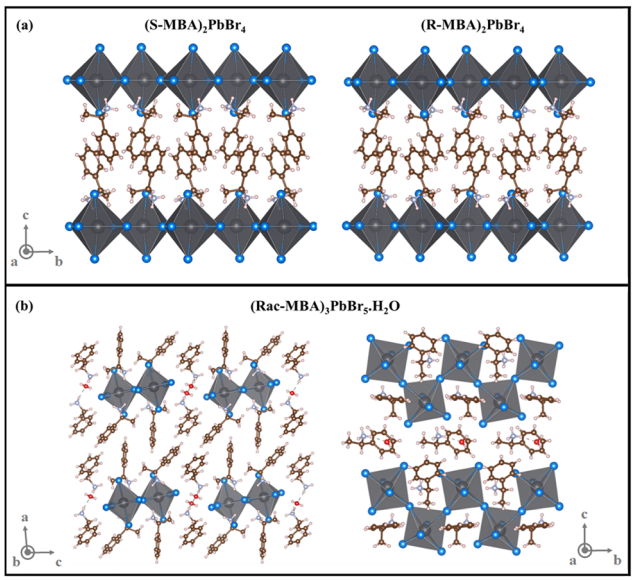

Fig. 2 (a) Crystal structures of the 2D perovskites (*S*-MBA)$_2$PbBr$_4$ and (*R*-MBA)$_2$PbBr$_4$. (b) (left) Schematic representation of the four families of PbBr$_6$ octahedra formed in the (Rac-MBA)$_3$PbBr$_5$·H$_2$O crystal, grouped according to the direction of local polar distortion (dipole) and molecular chirality. These blocks emerge due to opposing lattice strains imposed by alternating *R*- and *S*-enantiomers, which inhibit in-plane octahedral connectivity and promote an one-dimensional chain geometry. (right) 1D arrangement of (Rac-MBA)$_3$PbBr$_5$·H$_2$O.

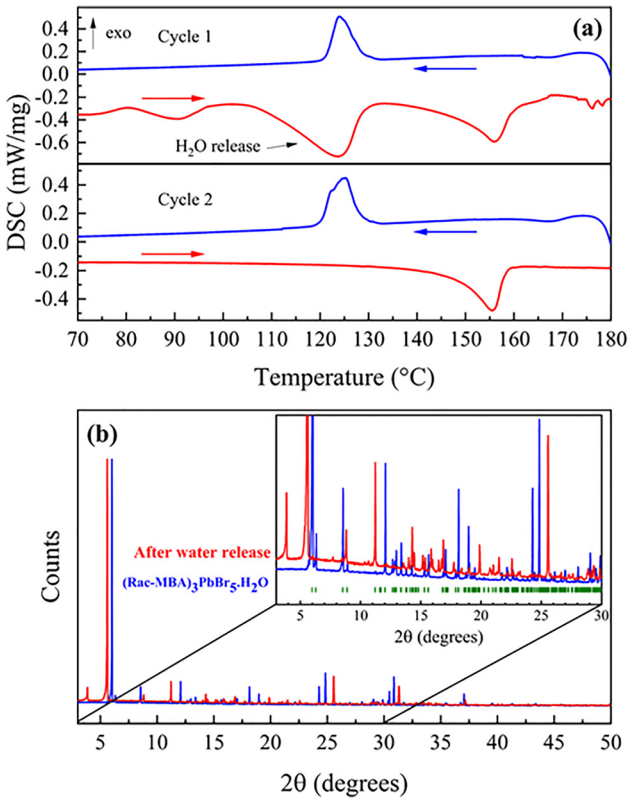

Fig. 3 (a) DSC data of (Rac-MBA)$_3$PbBr$_5$·H$_2$O performed at the first and second cycles. (b) Powder XRD of the as-grown (Rac-MBA)$_3$PbBr$_5$·H$_2$O and the new phase after water release from thermal treatment, both at room temperature. Green tick marks in the inset represent the expected Bragg reflection positions considering a monoclinic phase with *C*2/*c* space group symmetry of the hydrated perovskite.

in Fig. 2a, the presence of both *R*- and *S*-enantiomers disrupts this supramolecular order. In racemic systems, the coexistence of oppositely handed molecules leads to local dipole cancellation, introducing electrostatic inhomogeneity and long-range Coulombic repulsion between adjacent organic layers. Such electrostatic frustration, coupled with local steric mismatch, can distort the inorganic layers in such a way that inhibits the formation of periodic 2D hydrogen-bonded networks, leading to the reorganization into a lower-dimensional framework of corner-sharing PbBr$_6$ octahedra surrounded by radially reorganized MBA cations, as illustrated in Fig. 2b.[38,39]

To investigate the thermal stability of (Rac-MBA)$_3$PbBr$_5$·H$_2$O, we have performed differential scanning calorimetry (DSC) measurements on the hydrated perovskite in the temperature range of 65–180 °C, as shown in Fig. 3a (red and blue curves correspond to the heating and cooling processes, respectively). In the first heating cycle, a weak endothermic peak is observed beginning around 85 °C, likely associated with residual solution that remained even after cleaning. In addition, another endothermic event is observed starting around 110 °C, which may be associated with the removal of water from the monohydrated 1D perovskite structure as previously reported by Zhou *et al.* through thermogravimetric analysis (TGA).[40] A third endothermic peak appears at 150 °C during heating, followed by an exothermic event at 130 °C during cooling. In the second cycle, performed on the same sample, only the endothermic peak at 150 °C and the exothermic event at 130 °C are present during the heating and cooling processes, respectively, suggesting that an irreversible structural transformation of (Rac-MBA)$_3$PbBr$_5$·H$_2$O occurred due to the release of water. To confirm this phase transformation, we compared the room-temperature XRD patterns of the as-grown perovskite and the same sample after thermal treatment at 120 °C for 1 hour. As can be seen from Fig. 3b, the XRD patterns were markedly different, confirming the irreversible phase transformation indicated by the DSC data. We compared the XRD pattern of the new phase with those of the precursors (Rac-MBA)Br and PbBr$_2$, as well as the possible 1D and 2D phases of the MBA enantiomer-based perovskites, as shown in Fig. S3, further suggesting a new phase driven by water removal that will be determined elsewhere.

To understand the influence of molecular chirality and dimensionality on the electronic structure of these materials, we have performed DFT calculations for both the enantiopure and racemic systems. As expected from symmetry considerations, the *R*- and *S*-enantiomers yield identical band structures, with no discernible differences in electronic dispersion. The valence band maximum (VBM) primarily comprises Br p-orbitals in both cases. In contrast, the conduction band minimum (CBM) is dominated by Pb p-states, which agrees with previous reports on halide perovskites.[41,42] We corroborate

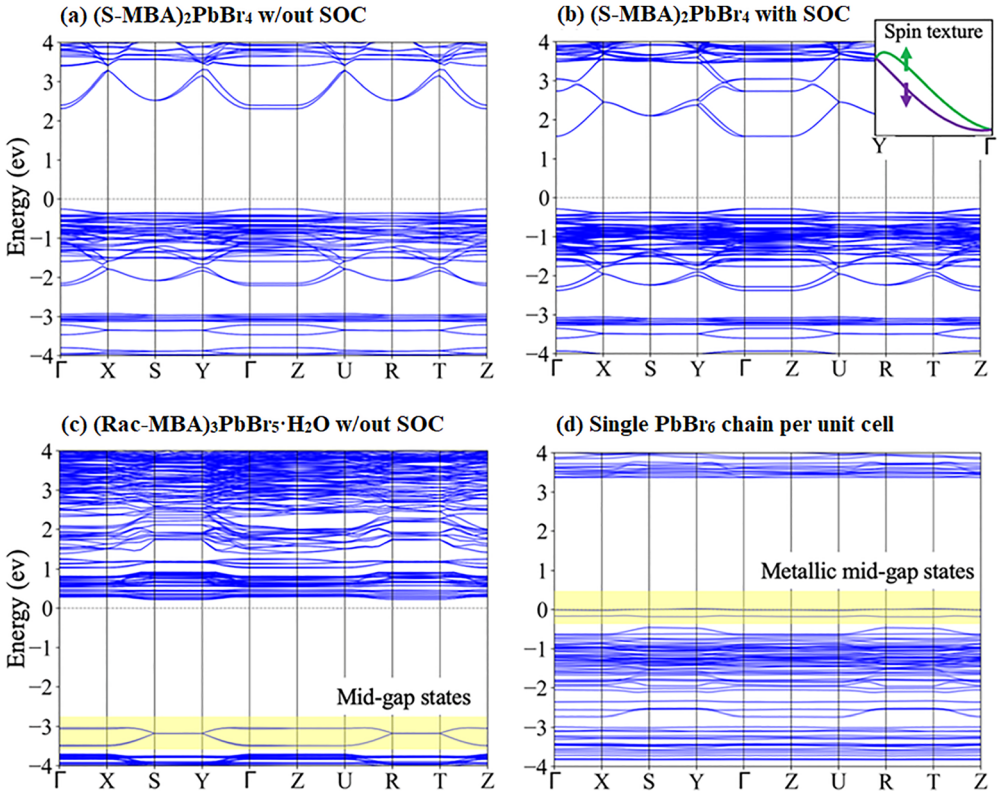

Fig. 4 Band structures of enantiopure and racemic lead bromide perovskites. (a) (*S*-MBA)$_2$PbBr$_4$ without spin–orbit coupling (SOC), showing a direct bandgap at Γ. (b) The same system with SOC, revealing Rashba-type spin splitting at the band edges (~10 meV). The inset shows the spin texture (expectation value of the spin operator), with opposite S_z orientations depicted in green and purple. (c) (Rac-MBA)$_3$PbBr$_5$·H$_2$O without SOC, showing mid-gap states from undercoordinated Br atoms and a Fermi level near the conduction band. (d) A reduced racemic system with a single PbBr$_6$ chain per unit cell, showing metallic behavior due to electrostatic instability.

this by *k*-resolved band-character projections, consistent with type-I band-edge ordering on the inorganic Pb–Br network. The calculated bandgap is direct and located at the Γ-point, with a value of approximately 2.8 eV using the PBE functional as shown in Fig. 4a. Although this functional is known to underestimate the absolute bandgap by about 1 eV,[43–45] the relative trends remain reliable. They will be discussed further in the next section. Notably, the inclusion of spin–orbit coupling (SOC) reveals a Rashba-like spin splitting at the conduction band minima, with a momentum offset and energy splitting on the order of 10 meV (Fig. 4b), as expected by the chiral-induced deformation in polar materials.[46] Polarization-resolved spectroscopic measurements would be required to isolate the microscopic origin of this splitting and to disentangle SOC-driven effects from possible optical phenomena such as photon recycling or bound exciton emissions.[47,48]

In contrast, the racemic compound (Rac-MBA)$_3$PbBr$_5$·H$_2$O exhibits a significantly reduced bandgap relative to its chiral counterpart. This narrowing originates from the mid-gap states derived from Br atoms that lack full coordination due to the disrupted octahedral connectivity in the one-dimensional structure. Although partially stabilized by hydrogen bonding with water molecules, these undercoordinated Br orbitals introduce electronic states deep within the gap region, as revealed in the unfolded band structure (Fig. 4c). Furthermore, the Fermi level lies very close to the conduction band edge, indicating that the hydrated racemic phase behaves as an extrinsic semiconductor—likely a consequence of charge compensation mechanisms facilitated by interstitial water molecules.

To assess the energetic role of the one-dimensional motif, we simulated a configuration where only a single PbBr$_6$ chain per unit cell is retained while maintaining water molecules in the lattice. We find that the total energy per atom increases by approximately 3 eV compared to the system containing the four symmetry-related chains with alternating chirality and polarization. This large energy penalty reflects the emergence of electrostatic instability due to the absence of inter-chain dipole compensation. In this reduced symmetry case, the system spontaneously becomes metallic to screen internal fields, a phenomenon reminiscent of surface electrical stabilization in ferroelectric materials[49] (Fig. 4d). Furthermore, we explored the effect of water removal by eliminating interstitial H$_2$O molecules from the racemic hydrated structure. In all configurations examined, the absence of water leads to a drastic increase in internal energy—by nearly an order of magnitude—indicating that hydration is critical to the structural and electronic stability of the system. These results suggest that upon thermal desorption of water, the material would likely undergo substantial atomic rearrangement to restore electronic balance and minimize electrostatic energy.

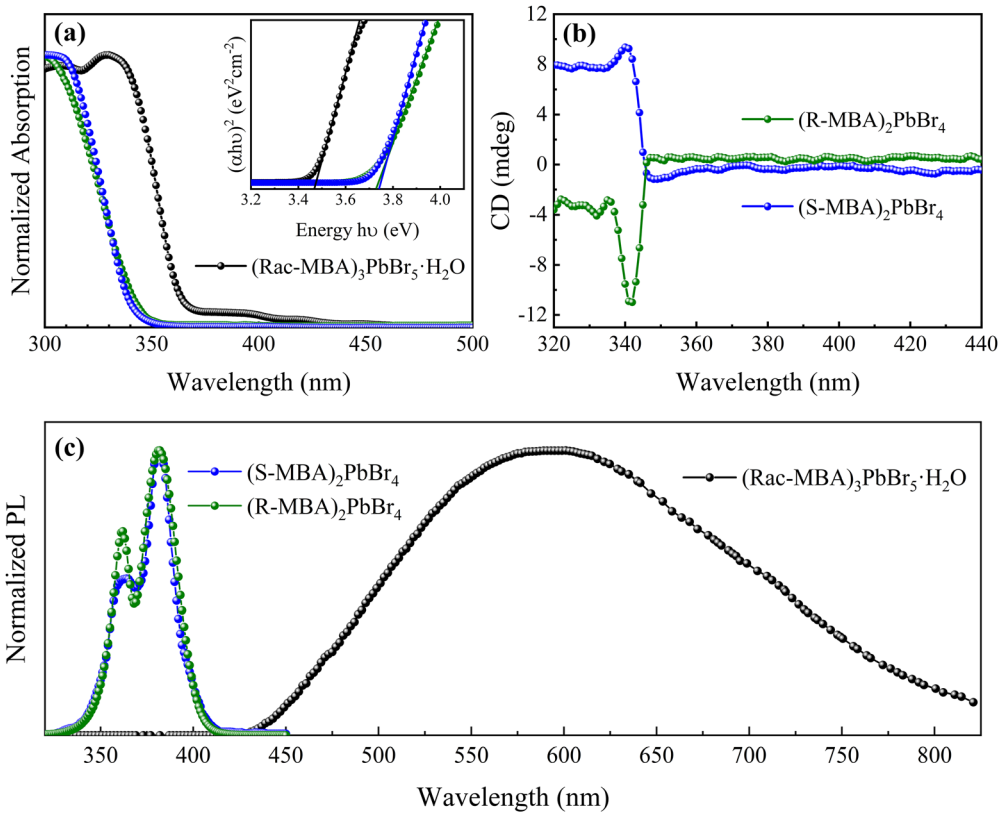

Fig. 5 Room-temperature optical properties of the (*R*-/*S*-MBA)$_2$PbBr$_4$ and (Rac-MBA)$_3$PbBr$_5$·H$_2$O perovskites. (a) Normalized absorption spectra with the Tauc plot in the inset. (b) Circular dichroism of the enantiomer-based perovskites. (c) Normalized photoluminescence spectra.

Fig. 5a presents the room-temperature UV-visible absorption spectra of (*R*-/*S*-MBA)$_2$PbBr$_4$ and (Rac-MBA)$_3$PbBr$_5$·H$_2$O crystals. The absorption edges are located at approximately 345 nm for the enantiomer-based compounds, consistent with previously reported absorption spectra of powder samples of these perovskites.[50] For the hydrated 1D phase, the absorption spectrum closely resembles that reported by Dang *et al.*,[21] featuring a small peak centered around 400 nm, which can be attributed to defect-induced mid-gap states, and a strong peak at 350 nm, commonly assigned to excitonic absorption. The direct band-gap energies were determined *via* the Tauc plot method to be 3.74 eV and 3.47 eV for the 2D and 1D perovskites, respectively. To confirm whether the incorporation of chiral ligands resulted in chiral perovskites, we performed circular dichroism (CD) spectroscopy on thin films obtained by dissolving the crystals in DMF and spin-coating them onto quartz substrates. This approach was necessary since the as-synthesized crystals were too thick to yield a reasonable CD response. As shown in Fig. 5b, CD signals were observed for (*R*-/*S*-MBA)$_2$PbBr$_4$ around 350 nm with oppositely signed values near the absorption edge for each sample, which can be attributed to the Cotton effect.[34,51] This proves that chirality was successfully transferred from the chiral ligands to the inorganic sublattices.

Steady-state photoluminescence (PL) spectra of the samples are shown in Fig. 5c. For the (*R*-/*S*-MBA)$_2$PbBr$_4$ compounds, two distinct narrow emissions were detected at 362 nm and 382 nm, both near the absorption edge. The higher-energy PL peak is widely attributed to free exciton emission in 2D halide perovskites,[52,53] whereas the origin of the lower-energy emission remains under debate. Possible explanations include photon recycling mechanisms, in which a portion of the high-energy emission becomes strongly confined within the crystal, aided by the 2D structural configuration. This confined light can propagate over long distances through total internal reflection, thereby enhancing photon recycling during emission transmission and resulting in a subsequent red-shifted emission, as previously reported for the 2D perovskites (BA)$_2$PbBr$_4$ and (PEA)$_2$PbBr$_4$.[48] Another possible mechanism involves spin splitting induced by SOC. Rashba-type splitting has been previously reported as the origin of the double emission feature in the 2D perovskite (PEA)$_2$PbI$_4$ and in other 3D hybrid perovskites.[54] As discussed earlier, the inclusion of SOC revealed a Rashba-like spin splitting at the conduction band minimum in (*S*-MBA)$_2$PbBr$_4$. However, the calculated energy splitting (~10 meV) is significantly smaller than the experimentally observed separation between the double-emission peaks (~180 meV), suggesting that additional mechanisms may also be involved. Nevertheless, the definitive assignment of the PL peaks in the (*R*-/*S*-MBA)$_2$PbBr$_4$ compounds would require further experimental analyses, such as power-dependent and time-resolved PL measurements.

An intriguing photoluminescence behavior is observed with the use of the racemic mixture. The (Rac-MBA)$_3$PbBr$_5$·H$_2$O 1D perovskite exhibits a broadband emission (BE) centered around

600 nm, commonly associated with self-trapped exciton (STE) emission in halide perovskites.[55,56] Similar broadband emissions are observed in the enantiomer-based 1D perovskites (*R*-/*S*-MBA)$PbBr_3$;[21] however, in this case the emission is redshifted compared to the racemic hydrated phase, which can be related to the differences in the octahedral connectivity of the $PbBr_6$ octahedra from the corner-sharing type for (Rac-MBA)$_3PbBr_5\cdot H_2O$ and the edge-sharing case for (*R*-/*S*-MBA)$PbBr_3$. This difference in connectivity can modify the orbital overlap of Pb–Br bonds and alter the conduction/valence bandwidths and effective mass, which in turn can affect how deeply an exciton could be localized in a STE state. The BE indicates STE recombination, facilitated by lattice softness, reduced dimensionality, and hydrated interchain environments. The emergence of STE luminescence in the racemic compound underscores the profound effect of dimensionality and molecular packing on exciton dynamics. Remarkably, an intriguing photophysical behavior emerges with the use of the racemic cations, which results in the formation of a 1D perovskite structure, (Rac-MBA)$_3PbBr_5\cdot H_2O$, instead of the 2D phase typically observed with the chiral (*R*- or *S*-MBA) analogs. The origin of this broadband emission can be attributed to a confluence of structural and electronic factors.[57,58] The use of a racemic mixture likely introduces local packing disorder and reduces overall lattice symmetry, which are known to promote lattice deformation and exciton self-trapping. In low-dimensional halide perovskites, such distortions are particularly impactful, as they can localize photoexcited carriers *via* enhanced exciton–phonon coupling mechanisms.[57,58] Furthermore, the dimensional transition from 2D to 1D significantly enhances exciton–phonon interactions due to reduced dielectric screening and stronger quantum confinement. This effect is further reinforced by interstitial water molecules, which are stabilized between the inorganic chains in the 1D structure. These water molecules can interact dynamically with the organic cations *via* hydrogen bonding, further softening the lattice and facilitating vibrational modes that support STE formation. The reduced bandgap observed for the 1D Rac-MBA perovskite (3.47 eV) compared to its 2D counterparts (~3.74 eV) also suggests enhanced electronic delocalization along the chain axis, which may aid in the relaxation of excitons to lower-energy self-trapped states.

Temperature-dependent photoluminescence (PL) measurements were performed to investigate the emission behavior of the (Rac-MBA)$_3PbBr_5\cdot H_2O$ sample, as shown in Fig. 6a. The BE observed at room temperature blueshifts and its intensity rapidly increases upon cooling up to 110 K and reaches saturation around 80–100 K. Below 80 K, the BE redshifts and its intensity decreases followed by the emergence of a narrow-band emission (NE) centered at 410 nm with minor emissions around 350–375 nm that exhibits a relatively large Stokes shift compared to the excitonic peak at 350 nm, but it correlates closely with the absorption feature near 400 nm as shown in Fig. 5a, suggesting that it originates from bound exciton emission associated with mid-gap defect states. The BE profile resembles strong overlapping emission bands as the temperature decreases. Although multiple-peak fitting was attempted, the uncertainty in the number of contributing peaks and their

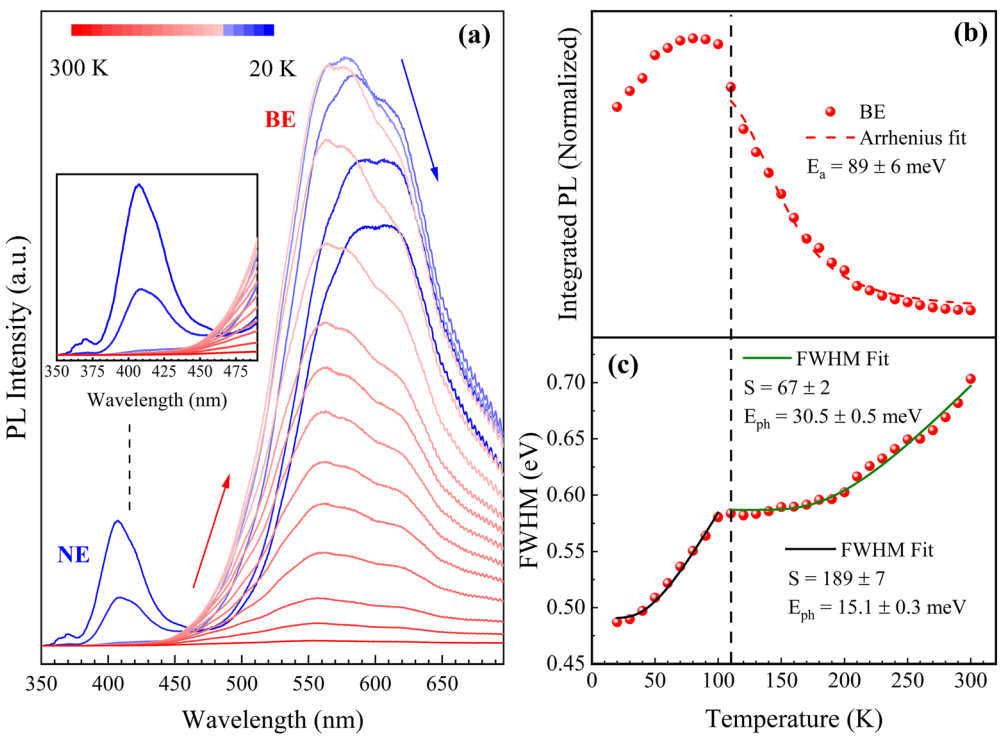

Fig. 6 (a) PL temperature dependence of (Rac-MBA)$_3PbBr_5\cdot H_2O$ perovskites. (b) Normalized integrated PL intensity and (c) the FWHM of BE dependence on temperature.

irregular shifts with temperature rendered the fitting results unreliable. As we have not observed well-resolved bands in the range of the NE emission, we have performed the analysis by considering the entire spectral range of the BE (450–700 nm) and NE (350–450 nm) regions to evaluate the following results.

The energy barrier that activates nonradiative processes, such as exciton trapping or nonradiative recombination, is referred to as the activation energy E_a and can be estimated by using the Arrhenius equation[59,60] applied to the integrated PL intensity $I_{PL}(T)$ dependence on temperature T according to eqn (1):

$$I_{PL}(T) = \frac{I_0}{1 + Ae^{\frac{-E_a}{k_B T}}} \quad (1)$$

where A is related to the density of radiative recombination centers, I_0 is the zero-temperature integrated intensity and k_B refers to the Boltzmann constant. Eqn (1) was applied to the integrated intensity of BE before saturation to obtain its activation energy as shown in Fig. 6b. To estimate E_a for the NE, due to the weak intensities at temperatures close to 110 K, we performed linear fitting of $\ln(I_0 I^{-1} - 1)$ as a function of $(k_B T)^{-1}$ as illustrated in Fig. S4. The results yield $E_a = 89 \pm 6$ meV for the BE and $E_a = 9.1 \pm 0.2$ meV for the NE. The activation energy for the BE can be related to the energy barrier for nonradiative recombination and is consistent with the presence of the broadband emission even at room temperature (thermal energy of ~25 meV). Since the emergence of the NE with increasing intensity occurs simultaneously with the reduction of the BE intensity, the low E_a value for the NE can be interpreted as the energy barrier for exciton trapping.[61] This interpretation is consistent with the appearance of the NE below 110 K (thermal energy of ~9.48 meV).

As before, the BE is attributed to STEs, which are closely related to the interactions between charge carriers and lattice vibrations. To assess the strength of the exciton–phonon coupling, we analyzed the temperature dependence of the BE linewidth $\Gamma(T)$, as shown in Fig. 6c. This dependence can be modeled using Toyozawa's theory,[62] which employs a configuration coordinate framework where the average number of phonons with effective energy E_{ph} emitted during exciton recombination is described using the Huang–Rhys factor S,[63] in the form of eqn (2):

$$\Gamma(T) = \Gamma_0 \sqrt{S} E_{ph} \sqrt{\coth\left(\frac{E_{ph}}{2k_B T}\right)} \quad (2)$$

where $S \gg 1$ typically indicates strong coupling.[64,65] Analysis of Fig. 6c reveals two distinct regimes above and below 110 K. Shifting the zero temperature to 110 K, to reflect thermally activated phonons, Toyozawa's model applied to the PL linewidth data above 110 K yielded $E_{ph} = 30.5 \pm 0.5$ meV (~245 cm^{-1}) and $S = 67 \pm 2$, which elucidates the strong exciton–phonon coupling usually found in STE emission. In contrast, the analysis below 110 K gives $E_{ph} = 15.1 \pm 0.3$ meV (~122 cm^{-1}) and $S = 189 \pm 7$. The effective phonon energies could be associated with those seen in the Raman spectrum at 143 cm^{-1} and 230 cm^{-1} as shown in Fig. S5, while the change in phonon energy is expected as higher-energy phonons become frozen out at low temperatures. Notably, the low-temperature Huang–Rhys factor (S) is 189 ± 7, which is almost three times higher than the high-temperature value and among the largest reported to date, to the best of our knowledge. The

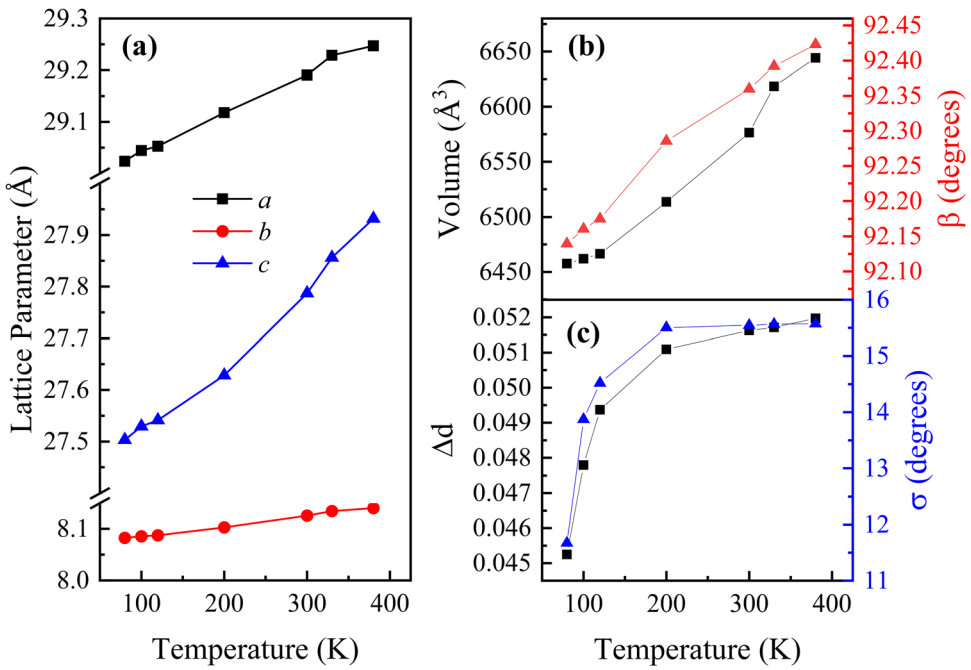

Fig. 7 Temperature dependence of the lattice parameters (a) a, b, c, and (b) β along with the unit cell volume of (Rac-MBA)$_3$PbBr$_5$·H$_2$O perovskites. (c) Behavior of octahedral distortions evaluated using the distortion index Δd and bond angle variance σ with temperature.

pronounced variation in the Huang–Rhys parameter S with temperature reflects changes in the effective phonon energy. Since S represents the average number of phonons emitted during recombination, higher-energy phonons require fewer phonons to facilitate the same transition, thereby reducing the value of S.[64]

In order to determine whether the changes observed in the photoluminescence were related to structural origins, temperature-dependent XRD measurements of (Rac-MBA)$_3$PbBr$_5$·H$_2$O powder were conducted, as shown in Fig. S6. Rietveld refinement of the diffractograms revealed a continuous decrease of the lattice parameters and unit cell volume from 380 K to 80 K, while the monoclinic crystal structure remained unchanged, as illustrated in Fig. 7a and b (see some selected temperatures in Fig. S7). These results exclude the possibility of structural phase transitions at low temperatures that could modify the electronic structure of the 1D perovskites and lead to different emission behavior.

To gain insights into the temperature behavior of the inorganic framework, the octahedral distortions were further analyzed using the distortion index $\Delta d = \sum_i |d_i - d|/6d$, where d_i is the ith Pb–Br bond length in an octahedron and d is the average bond length, and the bond angle variance $\sigma^2 = \sum_i (\theta_i - 90^\circ)^2 \Big/ 11$, where θ_i represents the ith Br–Pb–Br bond angle in an octahedron. As shown in Fig. 7c, the octahedral distortions slowly change above 120 K, which indicates the persistence of the octahedral configuration. However, the opposite trend is observed in the range of 120 K to 80 K, where octahedral distortions decrease with temperature. Octahedral distortions are known to contribute to the formation of self-trapped excitons (STEs), where more distorted environments are prone to exciton trapping.[55,66,67] However, lowering the temperature or applying pressure usually promotes exciton self-trapping by increasing octahedral distortions.[68,69] In contrast, we report an unusual case for (Rac-MBA)$_3$PbBr$_5$·H$_2$O, where lower temperature reduces octahedral distortions, and we propose that these distortions play a central role in governing the photoluminescence behavior of the hydrated 1D phase at low temperatures. Reduced octahedral distortions create a less favorable environment for exciton trapping, enabling the appearance of a high-energy narrow emission alongside the STE band, as not all excitons can be trapped within the more regular octahedral framework. Similar behavior has previously been observed in layered bromide perovskites under pressure.[70]

4. Conclusion

In this work, we revealed the influence of molecular chirality on the structural dimensionality and photophysical behavior of lead bromide hybrid perovskites. By systematically comparing enantiopure and racemic α-methylbenzylammonium (MBA) cations, we demonstrate that subtle changes in molecular stereochemistry can result in different crystallographic and optical properties. Enantiopure MBA cations promote the formation of highly ordered 2D Ruddlesden–Popper perovskites with orthorhombic symmetry, with narrow excitonic emission. In contrast, the racemic MBA mixture induces packing frustration that prevents layered ordering and favors the formation of a 1D hydrated phase, (Rac-MBA)$_3$PbBr$_5$·H$_2$O. This dimensional transition is accompanied by the emergence of broadband visible photoluminescence, attributed to the recombination of STEs. Temperature-dependent optical and structural studies reveal that this broadband emission arises from strong exciton–phonon coupling, facilitated by octahedral distortions in the 1D structure. These findings are further supported by DFT calculations revealing the emergence of mid-gap states in the racemic structure, arising from undercoordinated Br atoms, and a Fermi level pinned near the conduction band, consistent with extrinsic semiconducting behavior. In the chiral 2D phase, spin–orbit coupling induces Rashba-type spin splitting, highlighting the interplay between chirality and relativistic effects. Energetic comparisons confirm that both interstitial water and the complete set of symmetry-related 1D chains are essential for stabilizing the racemic hydrated phase, with removal of either leading to metallicity or electrostatic destabilization. Our findings demonstrate that racemic mixtures can be strategically exploited to access lower-dimensional frameworks and broadband emitters, expanding the design space for next-generation optoelectronic devices.

Author contributions

C. C. S. S. performed the synthesis, SEM, XRD, Raman, UV-visible absorption, and PL measurements at room temperature. A. T. performed circular dichroism. J. R. T. and Y. G. G. performed the temperature-dependent PL measurements. C. C. S. S. performed the temperature-dependent PL fitting. C. M. A. performed all theoretical calculations. M. A. P. G. and A. P. A. performed the SCXRD measurements and phase determination. F. F. F. performed the temperature-dependent XRD measurements and Rietveld refinements. C. C. S. S. and J. A. S. wrote the manuscript. All the authors contributed to the data analysis and manuscript revision. J. A. S. supervised the project. After analyzing the results, all authors approved the final version of the manuscript.

Conflicts of interest

There are no conflicts to declare.

Data availability

The authors confirm that the data supporting the findings of this study are available within the article and its supplementary information (SI). SI: Representation of organic cations, XRD patterns, Rietveld refinements, SCXRD data and Raman spectra. See DOI: **https://doi.org/10.1039/d5ma01061f**.

CCDC 2466728 contains the supplementary crystallographic data for this paper.[71]

Acknowledgements

The authors would like to acknowledge the financial support from Brazilian agencies FAPESP (2025/18214-4, 2025/03449-6, 2024/16896-8, 23/01313-4, 23/11265-7 and 2023/09820-2), CNPq (307778/2023-1, 407956/2022-0, 407954/2022-8, 406322/2022-8, 306827/2023-9, and 310353/2023-8), CAPES (88887.669776/2022-00 and Finance Code 001) and Funcap ((UNI-0210-00047.01.00/23, 07548003/2023). The authors are grateful for the support from the Experimental Multiuser Center Facilities (UFABC). The authors also acknowledge the financial support from the São Paulo Research Foundation (FAPESP) through the Research, Innovation and Dissemination Center for Molecular Engineering for Advanced Materials – CEMol (Grant CEPID No. 2024/00989-7). The authors also gratefully acknowledge the Multiuser Computational Center at UFABC (CCM-UFABC) for providing the computational resources used in this study.

References

1 J. Fan, W. Li, Q. Zhou, G. Yang, P. Tang, J. He, L. Ma, J. Zhang, J. Xiao, Z. Yan, A. Li and X. Han, *Adv. Funct. Mater.*, 2025, **35**, 2401017.
2 H. Dong, C. Ran, W. Gao, M. Li, Y. Xia and W. Huang, *eLight*, 2023, **3**, 3.
3 X. Liu, J. Li, X. Cui, X. Wang and D. Yang, *RSC Adv.*, 2022, **12**, 32925–32948.
4 E. A. Morais, N. A. M. S. Caturello, M. A. Lemes, H. Ferreira, F. F. Ferreira, J. J. S. Acuña, S. Brochsztain, G. M. Dalpian and J. A. Souza, *ACS Appl. Mater. Interfaces*, 2024, **16**, 4261–4270.
5 Q. Zhou, W. Li, J. Xiao, A. Li and X. Han, *Adv. Funct. Mater.*, 2024, **34**, 2402902.
6 M. Zhang, L. Zhao, J. Xie, Q. Zhang, X. Wang, N. Yaqoob, Z. Yin, P. Kaghazchi, S. Zhang, H. Li, C. Zhang, L. Wang, L. Zhang, W. Xu and J. Xing, *Nat. Commun.*, 2021, **12**, 4890.
7 X. Li, S. Aftab, S. Hussain, F. Kabir, A. M. A. Henaish, A. G. Al-Sehemi, M. R. Pallavolu and G. Koyyada, *J. Mater. Chem. A*, 2024, **12**, 4421–4440.
8 P. Gao, A. R. Bin Mohd Yusoff and M. K. Nazeeruddin, *Nat. Commun.*, 2018, **9**, 5028.
9 Y. Liu, S. Yuan, H. Zheng, M. Wu, S. Zhang, J. Lan, W. Li and J. Fan, *Adv. Energy Mater.*, 2023, **13**, 2300188.
10 D. Cortecchia, J. Yin, A. Petrozza and C. Soci, *J. Mater. Chem. C*, 2019, **7**, 4956–4969.
11 R. I. Sánchez-Alarcón, O. E. Solís, M. C. Momblona-Rincon, T. S. Ripolles, J. P. Martínez-Pastor, R. Abargues and P. P. Boix, *J. Mater. Chem. C*, 2024, **12**, 7605–7614.
12 A. Tofanello, A. L. M. Freitas, T. B. de Queiroz, A. Bonadio, H. Martinho and J. A. Souza, *J. Phys. Chem. Lett.*, 2022, **13**, 1406–1415.
13 G. Long, R. Sabatini, M. I. Saidaminov, G. Lakhwani, A. Rasmita, X. Liu, E. H. Sargent and W. Gao, *Nat. Rev. Mater.*, 2020, **5**, 423–439.
14 Y. Dang, X. Liu, B. Cao and X. Tao, *Matter*, 2021, **4**, 794–820.
15 H. Li, R. Cao, M. Tao, J. Jiang and Y. Xiao, *Chem. Sci.*, 2025, **16**, 4057–4065.
16 Z. Ding, Q. Chen, Y. Jiang and M. Yuan, *JACS Au*, 2024, **4**, 1263–1277.
17 M. Moroni, C. Coccia and L. Malavasi, *Chem. Commun.*, 2024, **60**, 9310–9327.
18 J. Son, S. Ma, Y.-K. Jung, J. Tan, G. Jang, H. Lee, C. U. Lee, J. Lee, S. Moon, W. Jeong, A. Walsh and J. Moon, *Nat. Commun.*, 2023, **14**, 3124.
19 J. Ahn, E. Lee, J. Tan, W. Yang, B. Kim and J. Moon, *Mater. Horiz.*, 2017, **4**, 851–856.
20 Y. Asensio, L. Olano-Vegas, S. Mattioni, M. Gobbi, F. Casanova, L. E. Hueso and B. Martín-García, *Mater. Horiz.*, 2025, **12**, 2414–2435.
21 Y. Dang, X. Liu, Y. Sun, J. Song, W. Hu and X. Tao, *J. Phys. Chem. Lett.*, 2020, **11**, 1689–1696.
22 H. Lu, Z. V. Vardeny and M. C. Beard, *Nat. Rev. Chem.*, 2022, **6**, 470–485.
23 A. A. Coelho, *J. Appl. Crystallogr.*, 2018, **51**, 210–218.
24 L. Krause, R. Herbst-Irmer, G. M. Sheldrick and D. Stalke, *J. Appl. Crystallogr.*, 2015, **48**, 3–10.
25 A. L. Spek, *J. Appl. Crystallogr.*, 2003, **36**, 7–13.
26 G. M. Sheldrick, *Acta Crystallogr., Sect. A: Found. Adv.*, 2015, **71**, 3–8.
27 G. M. Sheldrick, *Acta Crystallogr., Sect. C: Struct. Chem.*, 2015, **71**, 3–8.
28 O. V. Dolomanov, L. J. Bourhis, R. J. Gildea, J. A. K. Howard and H. Puschmann, *J. Appl. Crystallogr.*, 2009, **42**, 339–341.
29 K. Momma and F. Izumi, *J. Appl. Crystallogr.*, 2011, **44**, 1272–1276.
30 J. P. Perdew, K. Burke and M. Ernzerhof, *Phys. Rev. Lett.*, 1996, **77**, 3865–3868.
31 G. Kresse and J. Furthmüller, *Phys. Rev. B: Condens. Matter Mater. Phys.*, 1996, **54**, 11169–11186.
32 G. Kresse and D. Joubert, *Phys. Rev. B: Condens. Matter Mater. Phys.*, 1999, **59**, 1758–1775.
33 S. Dan, S. Paramanik and A. J. Pal, *ACS Nano*, 2024, **18**, 35644–35653.
34 L.-S. Yang, E.-C. Lin, Y.-H. Hua, C.-A. Hsu, H.-Z. Chiu, P.-H. Lo and Y.-C. Chao, *ACS Appl. Mater. Interfaces*, 2022, **14**, 54090–54100.
35 D. G. Billing and A. Lemmerer, *CrystEngComm*, 2006, **8**, 686–695.
36 A. Abhervé, M. Allain and N. Mercier, *Inorg. Chem.*, 2024, **63**, 5916–5923.
37 M. Li, F. Fang, X. Huang, G. Liu, Z. Lai, Z. Chen, J. Hong, Y. Chen, R. Wei, G.-H. Ning, K. Leng, Y. Shi and B. Tian, *Chem. Mater.*, 2022, **34**, 2955–2962.
38 M. K. Jana, R. Song, H. Liu, D. R. Khanal, S. M. Janke, R. Zhao, C. Liu, Z. Valy Vardeny, V. Blum and D. B. Mitzi, *Nat. Commun.*, 2020, **11**, 4699.
39 S. Maheshwari, M. B. Fridriksson, S. Seal, J. Meyer and F. C. Grozema, *J. Phys. Chem. C*, 2019, **123**, 14652–14661.

40 Y. Zhou, W. Li, X. Chen, X.-Z. Li, X.-J. Wang, B. Bai, Y. Chen and H.-H. Fang, *J. Mater. Chem. C*, 2022, **10**, 15424–15430.
41 S. Tao, I. Schmidt, G. Brocks, J. Jiang, I. Tranca, K. Meerholz and S. Olthof, *Nat. Commun.*, 2019, **10**, 2560.
42 E. Manousakis, *Phys. Rev. B*, 2023, **108**, 045130.
43 W. Kohn, Y. Meir and D. E. Makarov, *Phys. Rev. Lett.*, 1998, **80**, 4153–4156.
44 J. Klimeš, D. R. Bowler and A. Michaelides, *Phys. Rev. B: Condens. Matter Mater. Phys.*, 2011, **83**, 195131.
45 T. Björkman, A. Gulans, A. V. Krasheninnikov and R. M. Nieminen, *Phys. Rev. Lett.*, 2012, **108**, 235502.
46 C. Mera Acosta, E. Ogoshi, A. Fazzio, G. M. Dalpian and A. Zunger, *Matter*, 2020, **3**, 145–165.
47 M. C. Gélvez-Rueda, E. M. Hutter, D. H. Cao, N. Renaud, C. C. Stoumpos, J. T. Hupp, T. J. Savenije, M. G. Kanatzidis and F. C. Grozema, *J. Phys. Chem. C*, 2017, **121**, 26566–26574.
48 M. A. Lemes, C. C. Soares, E. A. Morais, Y. J. Onofre, M. P. F. de Godoy, C. W. A. Paschoal, J. J. S. Acuña, C. M. Acosta and J. A. Souza, *ACS Photonics*, 2025, **12**, 3815–3828.
49 K. Garrity, A. M. Kolpak, S. Ismail-Beigi and E. I. Altman, *Adv. Mater.*, 2010, **22**, 2969–2973.
50 C. Zhou, Y. Chu, L. Ma, Y. Zhong, C. Wang, Y. Liu, H. Zhang, B. Wang, X. Feng, X. Yu, X. Zhang, Y. Sun, X. Li and G. Zhao, *Phys. Chem. Chem. Phys.*, 2020, **22**, 17299–17305.
51 J. Ma, C. Fang, C. Chen, L. Jin, J. Wang, S. Wang, J. Tang and D. Li, *ACS Nano*, 2019, **13**, 3659–3665.
52 S. Guo, W. Mihalyi-Koch, Y. Mao, X. Li, K. Bu, H. Hong, M. P. Hautzinger, H. Luo, D. Wang, J. Gu, Y. Zhang, D. Zhang, Q. Hu, Y. Ding, W. Yang, Y. Fu, S. Jin and X. Lü, *Nat. Commun.*, 2024, **15**, 3001.
53 C. Yang, Q. Wei, Y. Gong, M. Long, G. Zhou, G. Xing and B. Wu, *J. Phys. Chem. Lett.*, 2023, **14**, 10046–10053.
54 E. Lafalce, E. Amerling, Z.-G. Yu, P. C. Sercel, L. Whittaker-Brooks and Z. V. Vardeny, *Nat. Commun.*, 2022, **13**, 483.
55 Y. Han, X. Cheng and B.-B. Cui, *Mater. Adv.*, 2023, **4**, 355–373.
56 C. Yang, Q. Wei, Y. Gong, M. Long, G. Zhou, G. Xing and B. Wu, *J. Phys. Chem. Lett.*, 2023, **14**, 10046–10053.
57 Md. Z. Rahaman, S. Ge, C.-H. Lin, Y. Cui and T. Wu, *Small Struct.*, 2021, **2**, 2000062.
58 A. Biswas, R. Bakthavatsalam, S. R. Shaikh, A. Shinde, A. Lohar, S. Jena, R. G. Gonnade and J. Kundu, *Chem. Mater.*, 2019, **31**, 2253–2257.
59 C. C. S. Soares, J. S. Rodríguez-Hernández, Mayra A. P. Gómez, D. M. Andrade, P. B. A. Fechine, A. P. Ayala and C. W. A. Paschoal, *J. Mater. Chem. C*, 2024, **12**, 16758–16765.
60 J. Deveikis, M. Giza, D. Walker, J. Liu, C. Wilson, N. P. Gallop, P. Docampo, J. Lloyd-Hughes and R. L. Milot, *J. Phys. Chem. C*, 2024, **128**, 13108–13120.
61 M. D. Smith, A. Jaffe, E. R. Dohner, A. M. Lindenberg and H. I. Karunadasa, *Chem. Sci.*, 2017, **8**, 4497–4504.
62 Y. Toyozawa, *Prog. Theor. Phys.*, 1962, **27**, 89–104.
63 M. de Jong, L. Seijo, A. Meijerink and F. T. Rabouw, *Phys. Chem. Chem. Phys.*, 2015, **17**, 16959–16969.
64 K. M. McCall, C. C. Stoumpos, S. S. Kostina, M. G. Kanatzidis and B. W. Wessels, *Chem. Mater.*, 2017, **29**, 4129–4145.
65 Y. Han, J. Yin, G. Cao, Z. Yin, Y. Dong, R. Chen, Y. Zhang, N. Li, S. Jin, O. F. Mohammed, B.-B. Cui and Q. Chen, *ACS Energy Lett.*, 2022, **7**, 453–460.
66 X. Wang, W. Meng, W. Liao, J. Wang, R.-G. Xiong and Y. Yan, *J. Phys. Chem. Lett.*, 2019, **10**, 501–506.
67 Z. Ma, F. Li, L. Sui, Y. Shi, R. Fu, K. Yuan, G. Xiao and B. Zou, *Adv. Opt. Mater.*, 2020, **8**, 2000713.
68 L. Zhang, L. Wu, K. Wang and B. Zou, *Adv. Sci.*, 2019, **6**, 1801628.
69 J. Jin, L. N. Quan, M. Gao, C. Chen, P. Guo and P. Yang, *J. Phys. Chem. C*, 2023, **127**, 3523–3531.
70 F.-F. Gao, Y. Qin, Z.-G. Li, W. Li, J. Hao, X. Li, Y. Liu, C. J. Howard, X. Wu, X. Jiang, Z. Lin, P. Lu and X.-H. Bu, *ACS Nano*, 2024, **18**, 3251–3259.
71 CCDC 2466728: Experimental Crystal Structure Determination, 2025, DOI: **10.5517/ccdc.csd.cc2nstw5**.